MICROROBOTS

Copyright © 2019
The Authors, some
rights reserved;
exclusive licensee
American Association
for the Advancement
of Science. No claim
to original U.S.
Government Works

Reconfigurable magnetic microrobot swarm: Multimode transformation, locomotion, and manipulation

Hui Xie[1]*†, Mengmeng Sun[1]†, Xinjian Fan[1]†, Zhihua Lin[1], Weinan Chen[1], Lei Wang[1], Lixin Dong[2,3]*, Qiang He[1]*

Downloaded from https://www.science.org at The Hong Kong University of Science and Technology (Guangzhou) on May 26, 2026

Swimming microrobots that are energized by external magnetic fields exhibit a variety of intriguing collective behaviors, ranging from dynamic self-organization to coherent motion; however, achieving multiple, desired collective modes within one colloidal system to emulate high environmental adaptability and enhanced tasking capabilities of natural swarms is challenging. Here, we present a strategy that uses alternating magnetic fields to program hematite colloidal particles into liquid, chain, vortex, and ribbon-like microrobotic swarms and enables fast and reversible transformations between them. The chain is characterized by passing through confined narrow channels, and the herring school–like ribbon procession is capable of large-area synchronized manipulation, whereas the colony-like vortex can aggregate at a high density toward coordinated handling of heavy loads. Using the developed discrete particle simulation methods, we investigated generation mechanisms of these four swarms, as well as the "tank-treading" motion of the chain and vortex merging. In addition, the swarms can be programmed to steer in any direction with excellent maneuverability, and the vortex's chirality can be rapidly switched with high pattern stability. This reconfigurable microrobot swarm can provide versatile collective modes to address environmental variations or multitasking requirements; it has potential to investigate fundamentals in living systems and to serve as a functional bio-microrobot system for biomedicine.

INTRODUCTION

Nature provides a repertoire of examples of living systems organized in a coordinated manner to solve complex problems and to complete tasks that transcend individual capabilities. For example, a colony of ants can collectively achieve complex tasks such as constructing nests (*1*) and gathering large prey (*2*); herrings swimming in a grid can successfully capture very alert and evasive copepods in a synchronized way. Inspired by natural swarming, a variety of artificial swarm robotic systems composed of relatively unsophisticated robots that can achieve local interaction–guided complex collective formations (*3*, *4*) or exhibit cognitive abilities in complex task sequencing (*5*) have been reported. These robot swarms can partly mimic natural living systems by developing advanced collective algorithms and large-scale decentralized systems that rely on decreasing price and increasing performance of drive and communication hardware.

Recently, micro- and nanorobots have demonstrated great potential for in-body diagnosis and treatment at the cellular or even molecular level, which requires a tiny robot with great precision and robustness (*6*). However, integrating drive and sensing functions into micro- and nanoscale robots remains a challenge. In addition, because of the limited capabilities of a single micro- and nanorobot, only a vast number of collaborative micro- and nanorobots with independent drive and locomotion capabilities would be able to treat internal parts and organs of the human body that were previously inaccessible or to offer high-contrast bioimaging of the disease site. Fortunately, colloidal systems composed of microscopic active agents provide a promising candidate to build such a micro- and nanorobot system. Powered by external magnetic fields (*7*–*10*), electric fields (*11*, *12*), light (*13*), or chemical reactions (*14*), self-propelled colloidal individuals can form a swarm-level out-of-equilibrium system via physical or chemical interactions rather than informatic communications in the macrorobotic swarm. Nevertheless, regulating swarming micro- and nanobot systems with high flexibility to implement tasks in dynamically changing environment remains challenging, because relevant fundamental mechanisms, swarm-environment interactions, and the highly flexible coordination strategies in response to environmental changes and task variations are still under investigation.

A simple interactive alignment among a large number of active entities leads to the emergence of large-scale collective behavior. Although, in theory, substantial progress has been made in understanding the collective behavior of out-of-equilibrium systems (*15*–*19*), quantifying the agent-agent interactions is still the central problem when attempting to reveal the guiding principle of swarm behavior. In addition, the rich and diverse collective self-organization of recently identified colloidal systems—such as clustering (*20*–*22*), flocking (*23*), schooling (*24*), and self-organizing dynamic structures (*9*, *10*, *25*, *26*) in forms of chain (*27*), ribbon (*28*, *29*), and vortex (*10*, *30*, *31*)—may provide some insights for understanding complex collective behaviors in living systems. Nevertheless, using the same colloidal system to mimic complex and varied collective behaviors of living systems remains a challenge. This may require us to further understand the relevant mechanisms and to develop appropriate actuation strategies to programmatically regulate agent dynamics and the interactions among the agents.

Here, we report a magnetic microrobot swarm that offers high flexibility to collectively perform multiple tasks in a confined environment through multimode transformation and locomotion. The experimental system was realized by using peanut-shaped hematite colloidal particles energized by an alternating magnetic field. Driven by different input

---

[1] State Key Laboratory of Robotics and Systems, Harbin Institute of Technology, 2 Yikuang, Harbin 150001, China. [2] Electrical and Computer Engineering, Michigan State University, East Lansing, MI 48824, USA. [3] Beijing Advanced Innovation Center for Intelligent Robots and Systems, Beijing Institute of Technology, Beijing 100081, China.
*Corresponding author. Email: xiehui@hit.edu.cn (H.X.); ldong@egr.msu.edu (L.D.); qianghe@hit.edu.cn (Q.H.)
†These authors contributed equally to this work.

magnetic fields, the individual microrobot exhibited multiple dynamic modes of oscillating, rolling, tumbling, and spinning, which in turn triggered a group of microrobots to self-organize into corresponding swarm formations of liquid, chains (rolling columns), ribbon (tumbling rows), and vortex, respectively. We uncovered the complex nontrivial dynamics and generation mechanisms of different swarms by developing discrete particle simulation and computational methods. By tuning the frequency of the rotating magnetic field and its polarization in a three-dimensional (3D) space, we obtained a series of well-controlled, fast, and reversible transformations among these four collective formations and demonstrated maneuverability of the swarms by high-precision trajectory tracking. Experiments demonstrate high adaptability and functionality of the microrobot swarm: complex locomotion in confined environments such as narrow paths and channels by reconfiguring into the chain formation, coordinated handling of heavy loads well beyond an individual's capability by aggregating into the ant colony–like vortex, and large-area synchronized manipulation by reconfiguring into the herring school–like ribbon procession.

RESULTS

System design

We addressed multimodal patterning, transformation, and locomotion of the swimming microrobotic swarms for applications of multitasking in complex environments. As shown in Fig. 1A, multiple desired modes of swarming behavior can be synthetically programmed in the same colloidal system by regulating the dynamics of the individuals. In the study, the microrobotic system consists of a large number of peanut-shaped hematite colloidal particles with a long axis length equal to 3 μm and a short axis of 2 μm (inset in Fig. 1A). The microrobot has a permanent moment m ($m \approx 7 \times 10^{-16}$ Am^2) along its short axis. In the absence of an external energization, the microrobots spontaneously aggregate into a mass because of their own magnetic dipole force. The external rotating magnetic field (section S1) can be circularly polarized in any plane of 3D space to excite the microrobots in different motion modes (e.g., oscillating, rolling, wobbling, tumbling, and spinning), which determine the interaction among the active agents. The onset of large-scale collective behavior significantly depends on such simple interaction, and changes in the individual's dynamics will trigger the emergence of various forms of self-organizing systems.

The microrobot system exhibited an evenly distributed configuration, called the liquid form (section S2), when a uniform vertical alternating magnetic field $\mathbf{H}_l(t) = H_l[\sin(\omega t)\mathbf{e}_z]$ energizes the microrobots to oscillate at a rate of V_l; here, H_l is the magnitude of $\mathbf{H}_l(t)$ (subscript l represents the swarm formation of liquid; hereafter, c, v, and r represent swarm formations of chain, vortex, and ribbon, respectively), ω is the angular frequency of the magnetic field, t is the time, and $\mathbf{e}_z$ is the unit vector along the z axis (hereafter, $\mathbf{e}_x$ and $\mathbf{e}_y$ is that along the x and y axes, respectively). Furthermore, when applying a circularly polarized rotating magnetic field in the x-z plane, given by $H_c(t) = H_c[\cos(\omega t)\mathbf{e}_x - \sin(\omega t)\mathbf{e}_z]$, the microrobots rolled and polymerized into connected chain arrays (procession is along the alignment direction with a velocity of V_c) because of the dipole and hydrodynamic interactions among them. Specifically, the adjacent chains can be merged to evolve into longer chains. In addition, the rotating magnetic field $\mathbf{H}_v(t) = H_v[\cos(\omega t)\mathbf{e}_x - \sin(\omega t)\mathbf{e}_y]$ in the x-y plane resulted in the spin motion of the microrobots. Dynamic vortex arrays that span the entire colloidal system eventually emerged with constant collisions and fusion among the spinning microrobots. The fusion of two neighboring vortices with the same polarity was observed over time, and the chirality of the vortices was easily transferred by varying the spin direction of individual agents. Last, ribbon arrays (a procession direction

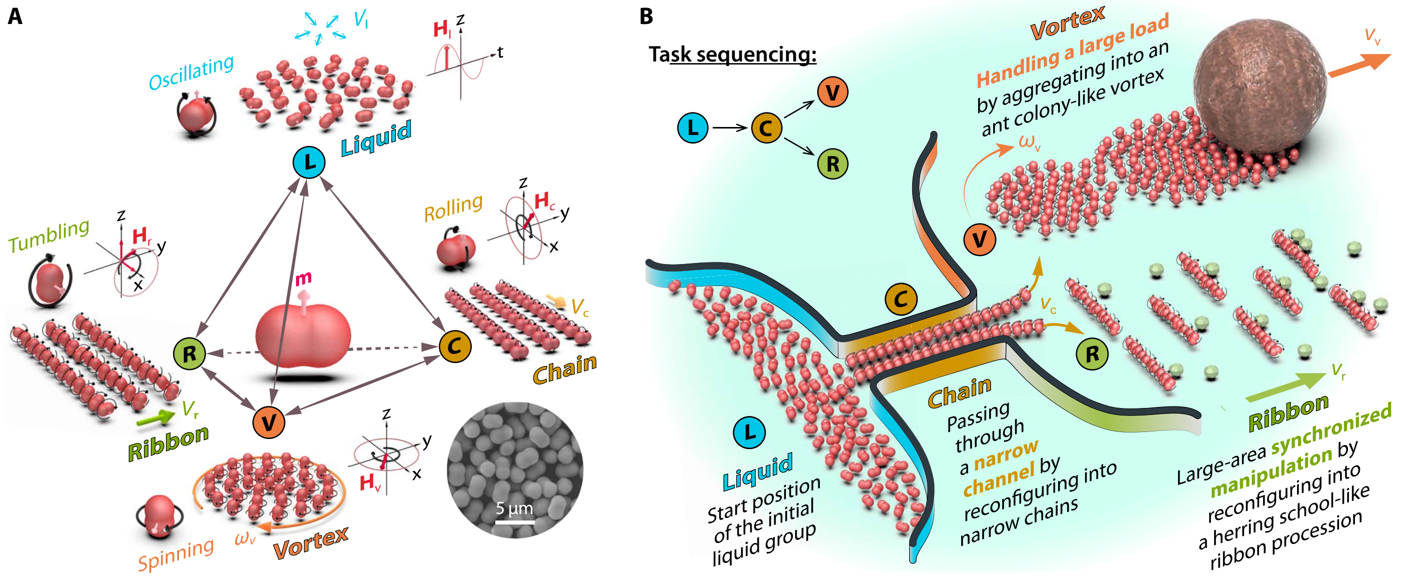

Fig. 1. Multimode transformations and collective manipulation. (**A**) Schematic of four programmable collective formations and the transformation between them. The hematite colloidal microrobots (inset) with the magnetic moment m were energized by alternating magnetic fields. The collective formations—liquid, chain, vortex, and ribbon—were programmatically triggered by alternating magnetic fields of $\mathbf{H}_l(t)$, $\mathbf{H}_c(t)$, $\mathbf{H}_v(t)$, and $\mathbf{H}_r(t)$, respectively. Moreover, it is possible to program the fast, reversible transition between these four formations. (**B**) Schematic showing collective manipulation capabilities of microrobotic swarms that emulate biological swarms: passing through a confined channel (C), handing large loads (V), and large-area synchronized manipulation (R) by reconfiguring into narrow chains, ant colony–like vortices, and a herring school–like ribbon procession, respectively.

Downloaded from https://www.science.org at The Hong Kong University of Science and Technology (Guangzhou) on May 26, 2026

perpendicular to the alignment with a velocity of V_r) were observed in a system of tumbling microrobots driven by a conical magnetic field $\mathbf{H}_r(t) = H_x\mathbf{e}_x + H_r[\cos(\omega t)\mathbf{e}_z - \sin(\omega t)\mathbf{e}_y]$; here, $\mathbf{H}_x$ is a DC component along the x axis. The ribbon, which consists of microrobots that are parallel to one another along their long axes, is an energetically favorable configuration due to the permanent magnetic moment. By reorganizing to follow the change in the magnetic field's polarization direction, all swarms in different formations can rapidly change their direction of motion. Moreover, because of the versatility of the mode transformation, the microrobotic system is capable of passing through the confined channel in the narrow chain formation, handling large loads (translation rate V_v) in the colony-like vortex formation (angular velocity ω_v) and large-area synchronized manipulation in the herring school–like ribbon procession (Fig. 1B).

Individual microrobot dynamics

To investigate the origin of the collective behavior, we first studied the dynamics of the individual microrobots in a very low concentration system, where the particle interactions are negligible. In the rotating magnetic field $\mathbf{H}_c(t)$, the microrobot rolled around its long axis (x axis) with a mean angular velocity of $\hat{\omega}$, owing to a magnetic torque equal to $\mathbf{T}_m = \mu_0(\mathbf{m} \times \mathbf{H})$; here, μ_0 is the vacuum permeability equal to $4\pi \times 10^{-7}$ Hm^{-1}. The microrobot cannot produce a net displacement in the reciprocal motion mode at low Reynolds numbers ($\mathrm{Re} \ll 1$) (*32*). Once there is a boundary at the bottom, the microrobot rolls along the surface because the apparent viscosity increases toward the surface. As shown in Fig. 2A, below a critical frequency ω_{cl} ($2\pi f_{cl}$), the velocity of the microrobot is proportional to the driving frequency, with $\hat{\omega} = \omega$. For $\omega > \omega_{cl}$, the microrobots can no longer follow the drive synchronously because of the marked increase in the liquid-induced viscous torque $T_{\text{visco}} = -8\pi\eta\hat{\omega}r^3$ (r is the equivalent radius of the microrobots and η is the fluid viscosity). In this case, $\hat{\omega}$ can be estimated by $\hat{\omega} = \omega\left(1 - \sqrt{(1 - (\omega_{c1}/\omega)^2)}\right)$. We observed that the chain often emerges in the low-frequency band (yellow region) within the sync area.

When applying the rotating magnetic field $\mathbf{H}_v(t)$, the microrobot rotated around the z axis. As the drive frequency increased, the angle θ between the microrobot's long axis and the z axis underwent a process of first decreasing and then increasing. A similar dynamical behavior of paramagnetic ellipsoidal particles has been observed under a conically rotating magnetic field (*33*). As shown in Fig. 2B, we quantified this process with a normalized projected area S/S_0; here, S_0 is the projected area occupied by the vertically rotating microrobot. The angle θ was about 90° at a frequency of 1 Hz, where the microrobot accounts for the largest projected area. At a frequency of about 20 Hz, θ decreased to 0, which resulted in the smallest projected area. When the frequency exceeded 30 Hz, θ increased from 0° to 90°, and the microrobot eventually laid down again on the surface. Our findings demonstrate that the frequency range of 15 to 75 Hz is the band (orange region) that is most effective for the emergence of the vortex.

The microrobots exhibited a tumbling motion under the conical magnetic field $\mathbf{H}_r(t)$. Because of the DC component $\mathbf{H}_x$, the microrobot rotated at a tilt angle ψ between its long axis and the rotating axis of the magnetic field, as shown in Fig. 2C. The precessing microrobot was

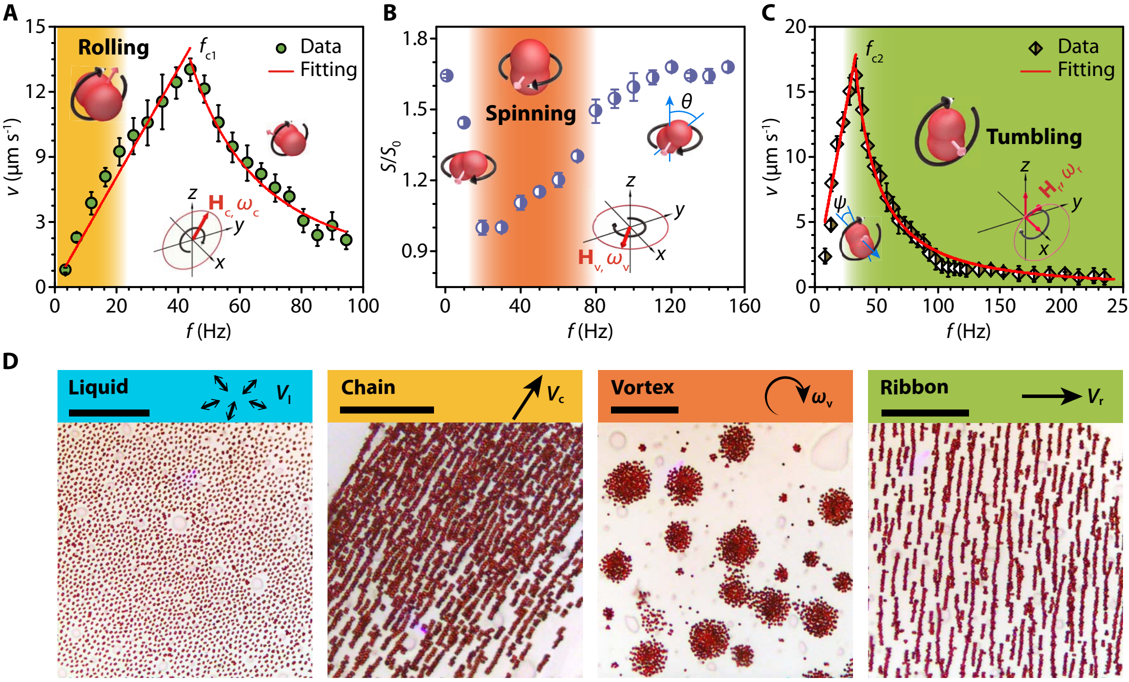

Fig. 2. Individual microrobot dynamics and corresponding collective formations. (**A**) Average velocity v versus the driving frequency f of a rolling microrobot (insets) subjected to a circularly polarized rotating field in the y-z plane (the bottom inset) with an amplitude of H_c = 4000 A m^{-1}. The yellow area indicates the formation interval of the chain (about 1 to 20 Hz). Error bars indicate SD. (**B**) The relationship between the projected area of a spinning microrobot (insets) and the input frequency. The orange area indicates the formation interval of a vortex (about 15 to 75 Hz) under the magnetic field $\mathbf{H}_v(t)$, which is characterized by H_v = 2000 A m^{-1} circularly polarized in the x-y plane. (**C**) Averaged velocity v as a function of driving frequency f of a tumbling microrobot (insets) subjected to a conical field ($H_r = H_x$ = 4000 A m^{-1}). The green area indicates the formation interval of the ribbon (about 25 to 250 Hz). (**D**) Snapshots (20×) from the left to right showing swarming patterns of the liquid (H_l = 4000 A m^{-1}, f = 10 Hz), chain (H_c = 4000 A m^{-1}, f = 5 Hz), vortex (H_v =2000 A m^{-1}, f = 30 Hz), and ribbon ($H_r = H_x$ = 4000 A m^{-1}, f = 150 Hz) in the microrobotic system. Scale bars, 50 μm.

Downloaded from https://www.science.org at The Hong Kong University of Science and Technology (Guangzhou) on May 26, 2026

characterized by a wobbling motion under a low frequency due to the rotation-translation hydrodynamic coupling. As the drive frequency increased, the microrobot motion gradually transitioned to tumbling mode due to the increase of the resistance. In addition, its translational velocity first increased and then decreased, with a critical frequency (f_{c2}) of about 34 Hz. Self-organization of the ribbon swarm was more likely to occur in the tumbling microrobot system. A wide frequency range of about 25 to 250 Hz is an effective band (green region) for the emergence of the ribbon.

When the density of the microrobots increased, neighboring agents started to interact. Each agent was subjected to a magnetic dipole force $\mathbf{F}^{m}$, a hydrodynamic thrust force $\mathbf{F}^{t}$, a repulsive force $\mathbf{F}^{r}$, a hydrodynamic attractive force $\mathbf{F}^{a}$ (only vortex), and a net force of gravity and electric repulsion $\mathbf{F}^{n}$ (see Materials and Methods). On the basis of Stoke's law (*34*), the microrobot was also subjected to a drag force when moving in a liquid with a velocity $\mathbf{u}$, given by $\mathbf{F}^{d} = 6\pi\eta a\mathbf{u}$. When the Reynolds number was low, a dynamic equilibrium among the abovementioned forces could be obtained

$$\sum_{\alpha=1,\beta\neq\alpha}^{N}\{\mathbf{F}^{m}_{\alpha,\beta}+\mathbf{F}^{t}_{\alpha,\beta}+\mathbf{F}^{r}_{\alpha,\beta}\}+\mathbf{F}^{a}+\mathbf{F}^{n}=\mathbf{F}^{d}=6\pi\eta a(\mathbf{v}-\mathbf{v}_{0}) \quad (1)$$

where α and β are indexes of the microrobots and $\mathbf{v}_0$ represents the mean velocity of an isolated microrobot that can be experimentally measured. The velocity $\mathbf{v}$ of the individual microrobot in an active system will be displaced with the velocity of the fluid flow (*25*). With this model, it is possible to accurately determine the complex dynamics of the individual microrobots. By tuning the magnetic field, we demonstrated all of the regimes depicted in Fig. 2D (movie S1).

Emergence of the programmable chain

Driven by the rotating magnetic field $\mathbf{H}_c(t)$, the two adjacent, rolling microrobots tended to interact because of the coupling of their fluid fields and magnetic dipole forces (see section S3). At low frequencies ($f \leq 20$ Hz), hydrodynamic interactions and the magnetic dipole forces within the coupling formed a dynamic equilibrium, which resulted in a stable rotating pair of microrobots that roll forward together (Fig. 3B, $t = 0.28$ and 2.10 s). As shown in the schematic diagram (Fig. 3A), the rotating pair was capable of trapping additional microrobots that were close to its trajectory, evolving into a tri-microrobot to more complex dynamic chain structures [Fig. 3B ($t = 2.74$ s) and movie S2].

The chain's generation mechanisms and collective motion were analyzed and simulated on the basis of the investigation of the magnetic attractive potential, hydrodynamic interactions, and viscous resistance (Eq. 1). Figure 3C shows the simulation results on the motion behaviors of a chain composed of three microrobots (A, B, and C) using LabVIEW. Unlike the "walking-like" motion and worm-like translation of the chain formed by paramagnetic colloid particles (*29*), the spatial trajectory of the microrobots in the x-z plane indicates that each microrobot (even the linked microrobots) experienced a "tank-treading" motion during the advancement of the chain. The microrobot's fluctuation on the z axis made a positional exchange possible, and the hopping advancement along the x axis resulted in the movement of the chain. As shown in Fig. 3D, this interesting behavior was observed by displaying the spatial positions of the microrobots on the x and z axes, separately. The seven typical phases, illustrated in the top and side views, describe the movement of the tri-microrobot chain during an entire motion cycle (movie S2). More complicated motion behavior was observed in the simulation results of the quad-microrobot chain (see section S4). Longer chains (more than 100 microrobots) emerged identically to the tri-microrobot one, except that the alternating motions among the microrobots and their forward transmission were more complicated.

Figure 3E shows the motion velocities (V_c) of chains composed of a different number of microrobots (N_s) under the same drive frequencies. Both the experimental (white square) and simulation data (blue dot) indicate that V_c increased rapidly as N_s increased to less than 6; then, the growth rate of V_c gradually decreased until it reached a specific stable value of about 6.5 μm s^{-1}. This finding is mainly due to the superposition of the flow field to produce a stronger thrust. This superposition effect is obvious with small N_s. As N_s increased, the effect became less pronounced because of the averaging effect. This phenomenon was also observed under different magnetic drive frequencies and strengths. In addition, Fig. 3F shows a linear increase in v_c of the trimer ($N_s = 3$) and the pentamer ($N_s = 5$) versus the magnetic field frequency (f). Error bars in Fig. 3 (E and F) represent the SD of the averaged values from three measurements. We experimentally observed that the motion of longer chains had the same response to the magnetic drive frequency.

Emergence of the programmable vortex

Under the external magnetic field $\mathbf{H}_v(t)$, the spinning microrobot produced a small vortex fluid field with itself as the vortex core. The spinning-induced hydrodynamic interaction and the time-averaged magnetic dipole forces attracted the microrobots to approach one another, and short-range repulsion kept the microrobots from getting too close to one another. A vortex was thus formed as more microrobots continue to aggregate. The process has been also demonstrated in the self-assembly of magnetic Janus particles into unusual crystals via rotating magnetic fields (*10*, *30*).

Snapshots in Fig. 4A show the growth process of vortices from the dispersion to the vortex state. The dynamic assembly of the vortex was significantly affected by the surface area fraction of the microrobots, because density-dependent diffusion in a nonequilibrium system leads to phase separations and an enormous number of fluctuations (*35*, *36*). At a given time of 60 s, only a few small vortices (less than five microrobots) were observed at the low fraction (φ = 2.08%), whereas large vortices emerged at a higher φ of about 11.99% (see section S5). The measured mean vortex size presented in Fig. 4B shows a transition from normal to a number of fluctuations above a critical surface fraction equal to φ = 6.90%. A slope of 0.22 was obtained by linearly fitting the measured mean vortex sizes against the surface area fraction below the critical value, whereas the slope above the critical surface fraction was 1.21. This significant difference indicates a phase separation in the vortex size growth, which is typical for the out-of-equilibrium system. Simulation results using COMSOL show a cross section of the velocity and vorticity distributions of a single particle as functions of the radius, and the velocity and vorticity maps of two, four, and six microrobots illustrate the fluidic interactions at the beginning of the vortex formation (Fig. 4C). Velocity distribution of a vortex is characterized by a linear azimuthal profile (Fig. 4D), which is in accordance with the simulation results. Using the developed discrete particle simulation method, we further simulated the generation process (lasting 15 s) of a vortex composed of 40 microrobots at a frequency of 20 Hz (Fig. 4E). The resulting snapshots show that a steady vortex was formed in 7.8 s (movie S3). The corresponding velocity fields demonstrated the coherent motion of the vortex (see section S6). Figure 4F shows an example of quickly transferring the vortex chirality from clockwise (CW) to counterclockwise (CCW) within 0.1 s

Downloaded from https://www.science.org at The Hong Kong University of Science and Technology (Guangzhou) on May 26, 2026

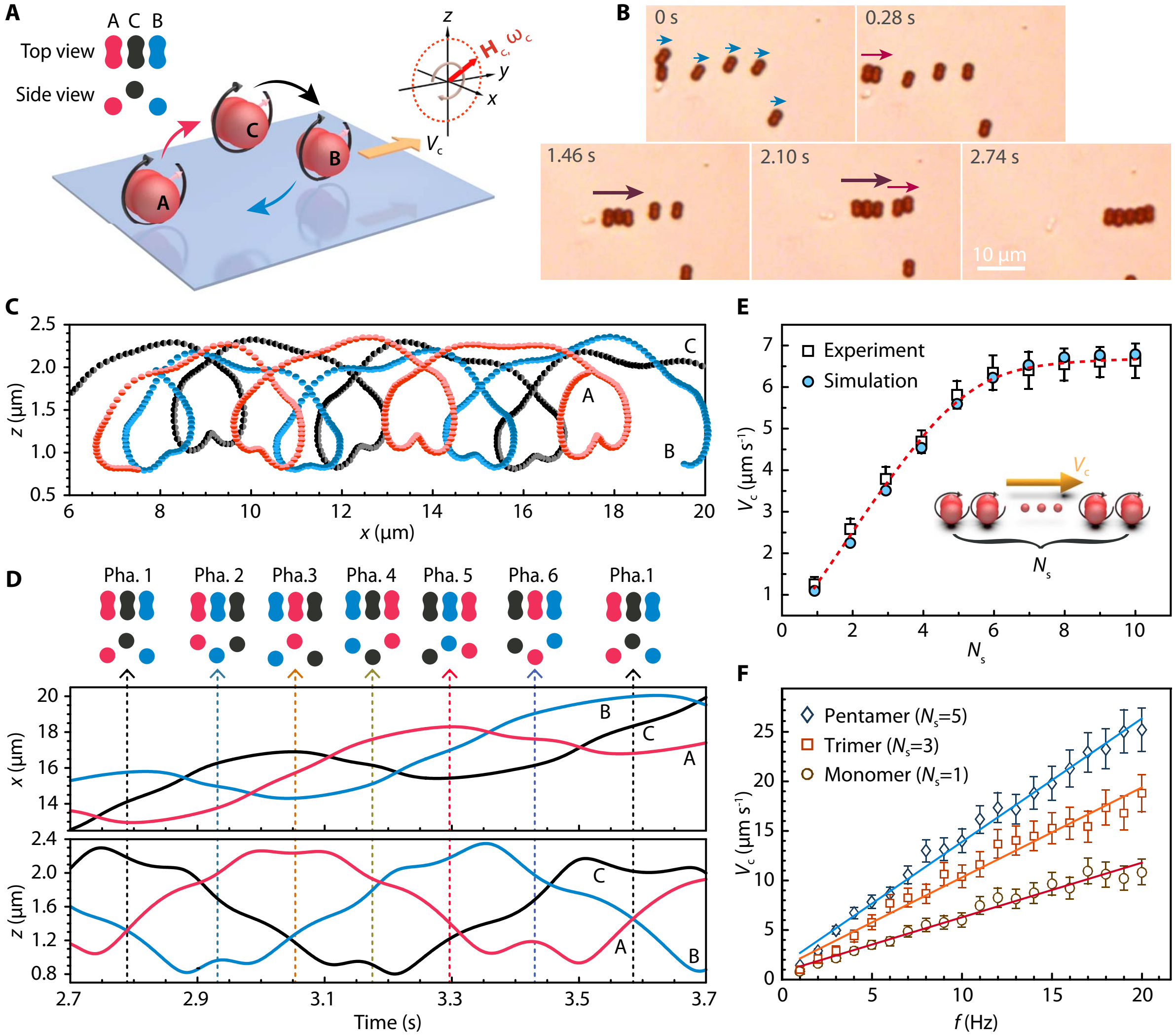

Fig. 3. Emergence of the programmable chain. (**A**) Schematic showing a typical tank-treading motion of a tri-microrobot chain subjected to a circularly polarized rotating magnetic field in the (*y*, *z*) plane. (**B**) Snapshots (40×) of the generation process of a five-microrobot chain under a rotating magnetic field (H_c = 8000 A m^{-1}, f = 5 Hz) (movie S2). Arrows indicate the motion direction. (**C**) Simulation results of the spatial trajectory of a tri-microrobot chain using LabVIEW. (**D**) Spatial positions of the microrobots on the *x* and *z* axes in one cycle. The seven typical phases presented in the top and side views depict the motion of the chain (movie S2). (**E**) Average velocity versus N_s (f = 4 Hz). (**F**) The chain's average velocity shows a linear relationship with the driving frequency (N_s = 1, 3, and 5).

by alternating the rotation direction of the magnetic field, which demonstrates that the programmed vortex exhibited good maneuverability and controllability. The chirality is further quantified by the polar order parameter ϕ_R; here, $\phi_R(t) = \frac{1}{N_s}\sum_{i=1}^{N_s}\mathbf{e}_{\varphi i}\cdot v_i(t)$ ($\mathbf{e}_{\varphi i}$ and v_i are the in-plane unit vectors in angular directions and unit velocities of the individual microrobots, respectively) (*22*). Regardless of whether the rotation was CW or CCW, the vortex was characterized by a high polar order parameter value of about 0.76, which is close to the ideal global polar state. The vortex in our experiment was a controlled reproducible system; its emergence did not depend on the presence of constraints or geometrical boundaries.

As a dynamic integral system, the vortex exerted long-range attractive forces on neighbors, resulting in vortex fusions. The simulation result and the experimental observation (Fig. 4G) demonstrate that the merging process typically includes three stages: exchange, fusion, and stabilization (movie S4). First, once the vortices were close enough, the nearest parts of the two vortices began to exchange members. Second, all the members entered the fusion zone to form an irregularly shaped vortex. Eventually, a large stable circular vortex that fused all members of the two vortices was formed. By swallowing small vortices into a main vortex one by one along a spiral trajectory, a giant vortex of more than 300 μm in diameter was formed in a few minutes, which contained more than 10,000 microrobots (section S7 and movie S5).

Emergence of the programmable ribbon

The microrobots exhibited a tumbling motion under the conical magnetic field $\mathbf{H}_r(t)$. The component $\mathbf{H}_x$ orients the permanent moment of the microrobots along the *x* axis, which facilitated the spontaneous assembly of a lateral ribbon along the magnetization direction. Adjacent tumbling microrobots were subjected to hydrodynamic and magnetic dipole forces. The hydrodynamic force first captured the microrobots in the vicinity. When entering the magnetic dipole attraction range, the trapped microrobots were closely aligned along the short axis of polarization and lastly assembled into a ribbon (Fig. 5A), which was

Downloaded from https://www.science.org at The Hong Kong University of Science and Technology (Guangzhou) on May 26, 2026

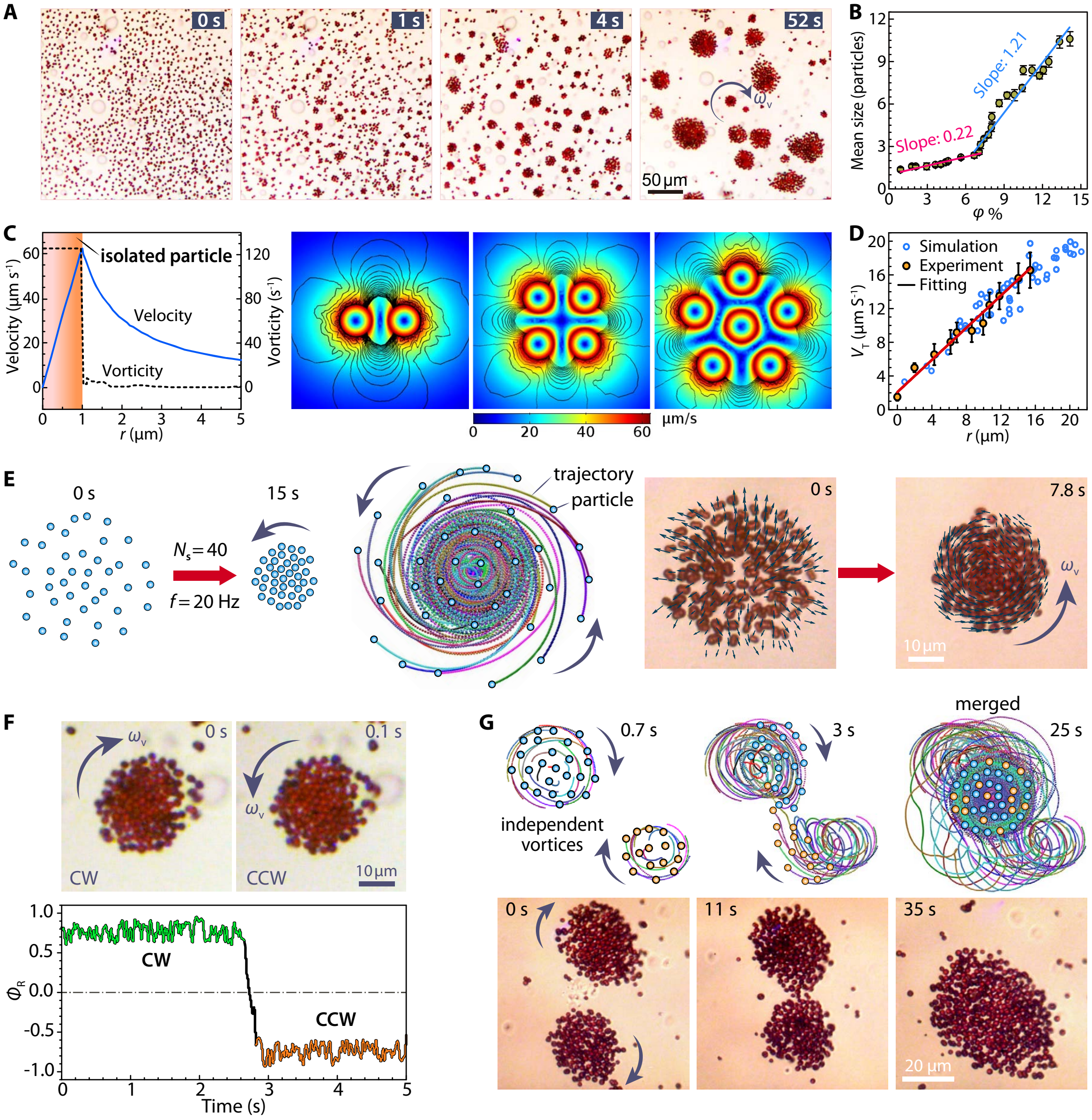

Fig. 4. Emergence of the programmable vortex. (**A**) Snapshots (20×) of the growth process from dispersion ($t = 0$ s) to the vortex state ($t = 52$ s) ($f = 30$ Hz, $H_v = 6000$ A m^{-1}). (**B**) Experimental results showing the average size of the vortex as a function of the critical surface fraction φ ($f = 30$ Hz and $H_v = 6000$ A m^{-1}). Error bars represent the SD of the averaged values from three measurements. (**C**) Simulation results showing a cross section of the velocity and vorticity distributions of a single particle as functions of the radius and the velocity and vorticity maps of two, four, and six microrobots at the beginning of the vortex formation. (**D**) The linear azimuthal velocity (V_t) profile of the vortex. r is the diameter. (**E**) Simulation result of the vortex generation process with the developed discrete particle simulation method and snapshots (40×) of the experimental result from dispersion ($t = 0$ s) to final vortex state ($t = 7.8$ s) ($f = 30$ Hz, $H_v = 6000$ A m^{-1}). (**F**) Snapshots (20×) that display the chirality switch of a vortex from CW to CCW rotation ($f = 30$ Hz and $H_v = 6000$ A m^{-1}). Rapid evolution of the polar order parameter φ_R verifies the controllability of the vortex chirality switching. (**G**) Simulation of the merging process of two neighboring vortices using the developed particle simulation approach ($f = 30$ Hz) and snapshots (40×) of the experimental result ($f = 30$ Hz, $H_v = 8000$ A m^{-1}).

previously demonstrated using ferromagnetic ellipsoids (*29*). Figure 5B presents snapshots of the generation process of a ribbon that consisted of six microrobots (movie S6); as seen, the dispersed microrobots were first polymerized into three pairs and then evolved into a hexamer.

To investigate the emergence of the ribbon, we used the developed computational model (see Materials and Methods) to simulate the role of the flow field around the tumbling microrobot. A streamplot of the flow velocity in the profile (on the *x*-*y* plane) shows the fluid approaching the ribbon ($N_s = 6$) from left and then pulling out to the right (Fig. 5C). Therefore, the flow was an attractive force behind the ribbon but a repulsive force in front of it. Figure 5D shows the flow velocity in the 3D profile, in which the distribution of the flow velocity is significantly different at the ends (characterized by a V-shaped trajectory) and the middle of the ribbon (characterized by a straight trajectory). The velocity field was calculated at the profile 1 μm above the ribbon.

Downloaded from https://www.science.org at The Hong Kong University of Science and Technology (Guangzhou) on May 26, 2026

By adding silver tracer particles (diameter, 1 μm), the motion trajectories of the fluids at different positions relative to the ribbon were also experimentally investigated. Experiment results in Fig. 5E demonstrate that the tracer particles in the flank of a ribbon (located at the top left and bottom left of the ribbon) were obliquely attracted to the ribbon first and then were pushed away by the water flow with a V-shaped trajectory. In contrast, the tracer particle located directly behind the ribbon was attracted along a straight line and then pushed away in the moving direction of the ribbon. The experimental observation (movie S6) is consistent with the simulation.

Figure 5F shows the motion velocities (V_r) of ribbons with different N_s values under the same drive frequencies. The experimental data indicate that V_r underwent a process of first increasing and then stabilizing as N_s increased. This phenomenon is also due to the combination of the enhancement of the flow field superposition and the average effect. In addition, Fig. 5G shows the relationship in V_r of the pentamer ($N_s = 5$) versus the magnetic field frequency (f) under different drive strength. Error bars represent the SD of the averaged values from three measurements. Similar to tumbling individual microrobot dynamics, changing the drive frequency could transform the ribbon dynamics from a synchronous regime to an asynchronous one. We experimentally observed that the motion of ribbons can be controlled precisely because of this characteristic.

Multimode transformations

Changes in the external magnetic field stimulus can break the original collective state and create a new dynamic steady state for the system. Our experiments have demonstrated that, by programmatically varying the external drive magnetic field, fast and reversible transformations can be accomplished between four swarming patterns mentioned above, which include a total of twelve transformations.

Figure 6A shows time-lapse image snippets (movie S7) that illustrate the process of programmatically reforming the microrobot swarms from liquid, vortex, and ribbon states to the chain. The transition started immediately when the magnetic field began switching, and the entire process lasted from a few seconds to 12 s. The density of the formed chains from the liquid state was relatively low because of the lower concentration. In contrast, the vortex-to-chain transition presented a

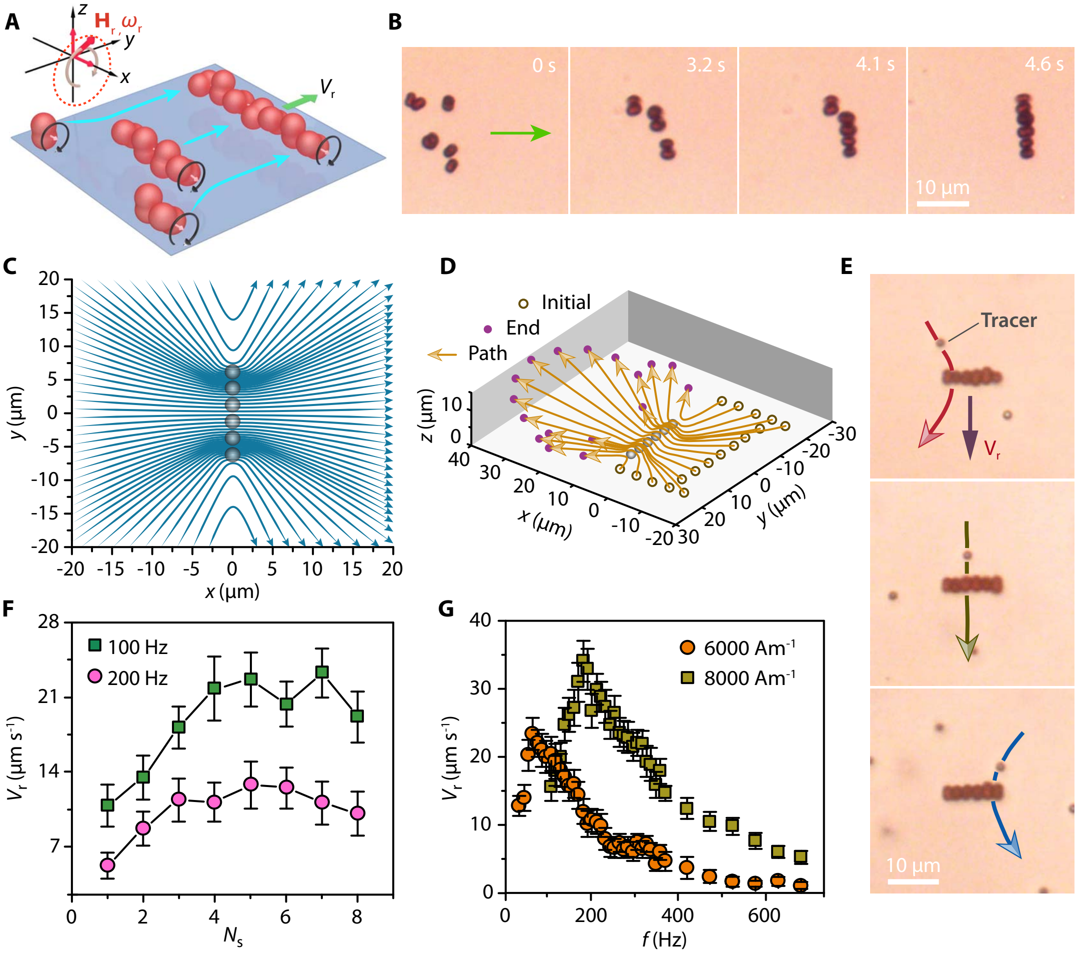

Fig. 5. Emergence of the programmable ribbon. (**A**) Schematic showing a generation process of a ribbon subjected to a circularly polarized rotating magnetic field in the (y, z) plane. (**B**) Snapshots (40×) showing the emergence of a six-microrobot ribbon under a precessing field ($H_r = 4000$ A m^{-1}, $H_x = 4000$ A m^{-1}, and $f = 200$ Hz) (movie S6). (**C**) Simulated flow streamlines on the (x, y) plane generated by a ribbon ($N_s = 6$) translating from left to right. (**D**) Simulation results of the 3D motion trajectory of the tracer particles. (**E**) Snapshots (40×) showing the motion of a tracer particle (diameter, 1 μm). (**F**) Average velocity versus N_s at different frequencies ($f =$ 100 Hz, $f = 200$ Hz) and the same magnitude $H_r = H_x = 4000$ A m^{-1}. (**G**) Average velocity of a ribbon versus driving frequency under two input fields of different strengths, where $H_{r1} = H_{x1} = 6000$ A m^{-1} and $H_{r2} = H_{x2} = 8000$ A m^{-1}.

Downloaded from https://www.science.org at The Hong Kong University of Science and Technology (Guangzhou) on May 26, 2026

scenario in which dense and long chains formed instantly and moved forward together for a long time to disperse into a stable density. The transition exhibited excellent dynamic performance, especially in the ribbon-to-chain transition, where the chains rapidly formed and aligned perpendicular to the initial ribbon. When the rotating direction of the external magnetic field changed drastically, the long chains reassembled instantly into a new alignment. Because of this excellent maneuverability, the chain could be programmed to steer in any direction.

Figure 6B shows a series of time-lapse image snapshots (movie S8), which illustrate the reforming process of the ribbon swarm from liquid, vortex, and chain. As expected, the density of the ribbon formed by the liquid was relatively low because of the lower concentration. In contrast, the vortex-to-ribbon transition immediately produced significant dense ribbons that underwent lateral rolls back and forth several times before being dispersed into a lower density. In the chain-to-ribbon transition, the ribbon was rapidly formed at a density similar to that of the chain. The long ribbon could reassemble rapidly in a new alignment to follow the varying magnetic field. Like chains, these highly maneuverable ribbons could be programmatically steered in any direction.

Programmable transformations from the liquid, ribbon, and chain to the vortex are shown in Fig. 6C (movie S9). The transformation from the liquid to the vortex took longer than transformations to the other

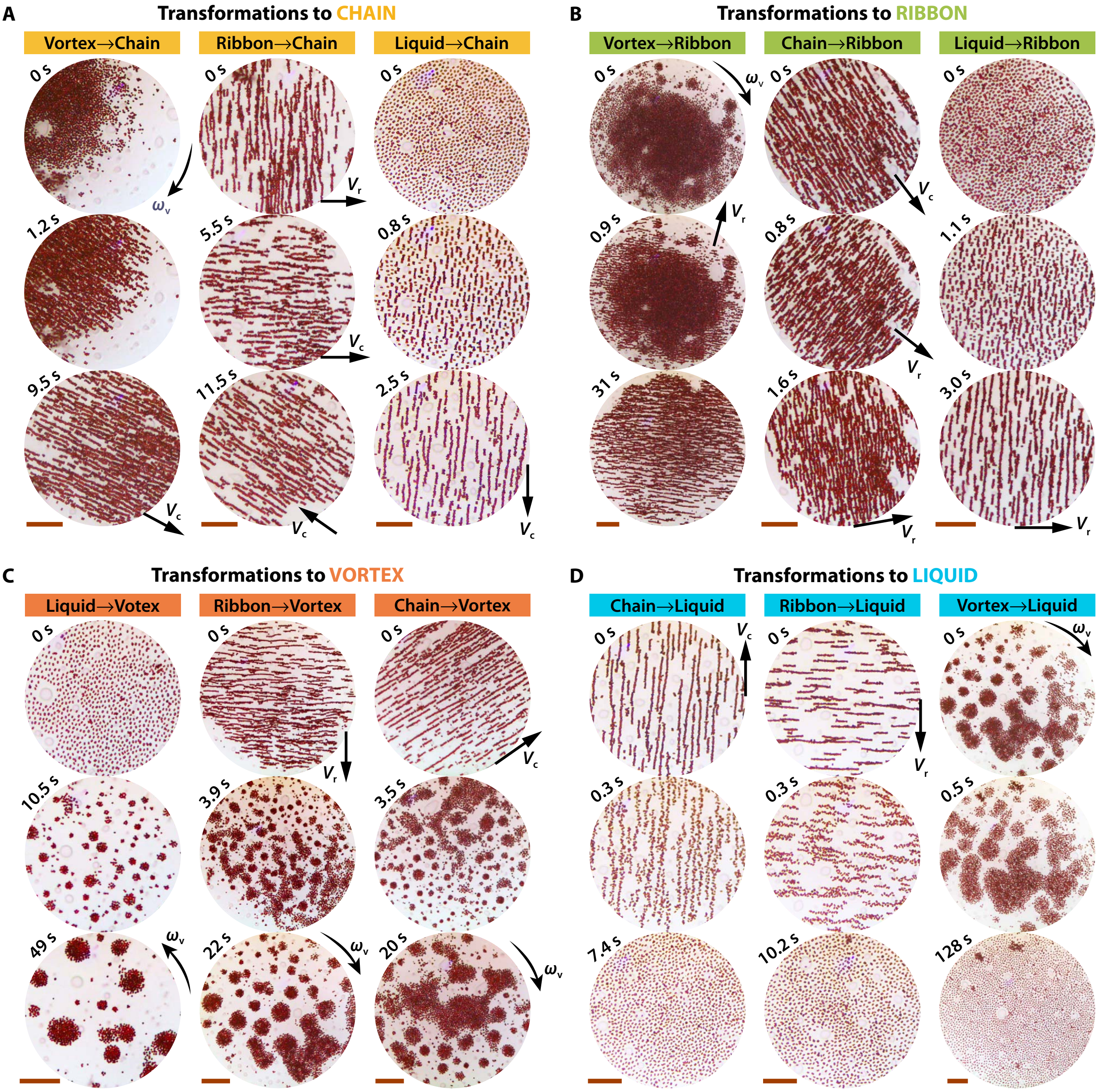

Fig. 6. Programmable multimode transformations. (**A**) Snapshots showing transformations to the chain from liquid, vortex, and ribbon states. (**B**) Sequence of images showing the transformations to the ribbon from liquid, vortex, and chain. (**C**) Image sequence showing the transformations to the vortex from liquid, ribbon, and chain. (**D**) Image sequence showing the transformations to the liquid from chain, ribbon, and vortex. Scale bars, 50 μm.

Downloaded from https://www.science.org at The Hong Kong University of Science and Technology (Guangzhou) on May 26, 2026

two collective states. This finding is mainly due to the small gap between the individuals in the chain and the ribbon, which saves time for reaggregation. However, because of uneven and dense microrobot distribution, large vortices with irregular shapes often emerged in the transitions from both the ribbon and the chain, whereas a uniform vortex array typically occurred in the transition from the liquid. In addition, more than one vortex (in the field of view) was often observed in all of the transitions, and merging phenomena among neighboring vortices were exhibited.

Transformations from the other three modes to liquid were relatively simple, and there were no complex dynamic changes. Once the oscillating magnetic field H_l was applied, the microrobots suddenly dispersed from the original patterns and gradually formed a uniform distribution, as shown in Fig. 6D (movie S10). The transformation from the chain and ribbon to liquid was faster than that from the vortex, which is due to the larger density of the vortex. The vortex-to-liquid transformation presented a distinct firework-like behavior that lasted for more than 100 s until all were completely dispersed.

Navigated locomotion

To evaluate the swarm's mobility, as well as its localization and tracking accuracy, we performed tasks of vision-navigated trajectory tracking with the small chain and vortex and ribbon swarms. Because the inertial force can be neglected at low Reynolds numbers, the swarms could be modeled as a first-order kinematic system (see Materials and Methods). Thus, by changing the steering angle α and frequency of input magnetic field, the swarms could be navigated to targets along a planned path (Fig. 7A). During the navigation, the microrobot swarms' velocities were indirectly regulated by tuning the frequency of the input magnetic field. In addition, considering the stability and efficiency of the steering of the swarm, the upper limit of the steering angle α for each adjustment was set at 20°. In addition to the frequency, the angle γ between the rotating magnetic field and the x-y plane could also be used to adjust the translational velocity of the vortex. However, to ensure the stability of the vortex, the angle γ was generally set to a fixed value between 15° and 20°.

A microrobot swarm navigated from the current position (x_c, y_c) to the reference position (x_r, x_r) along a planned path via the control scheme

$$v = k\min\left(\sqrt{e_x^2 + e_y^2} + f_{\min}, f_{\text{stepout}}\right)$$
$$\Delta\alpha = \begin{cases} \arctan\left(\frac{e_x}{e_y}\right) & \text{if} \quad \arctan\left(\frac{e_x}{e_y}\right) < 20^\circ \\ 20^\circ & \text{if} \quad \arctan\left(\frac{e_x}{e_y}\right) \geq 20^\circ \end{cases} \tag{2}$$

where $e_x = x_c - x_r$, $e_y = y_c - y_r$, $f_{\max}$ is the upper limit of the driving frequency, and $f_{\min}$ is the minimum driving frequency capable of overcoming Brownian motion of the microrobot or other external disturbance.

The locomotion navigation was performed using the entire closed-loop controller (section S8 and movie S11). Figure 7 (B to D) shows the locomotion results of the chain, vortex, and ribbon in tracking planned paths of a pentagon, circle, and rectangle, respectively. Figure 7E shows the corresponding distribution histograms of tracking errors, which demonstrate that the swarms can achieve high-precision path tracking with high maneuverability and pattern stability. In contrast, the tracking accuracy of the ribbon and the chain is relatively higher,

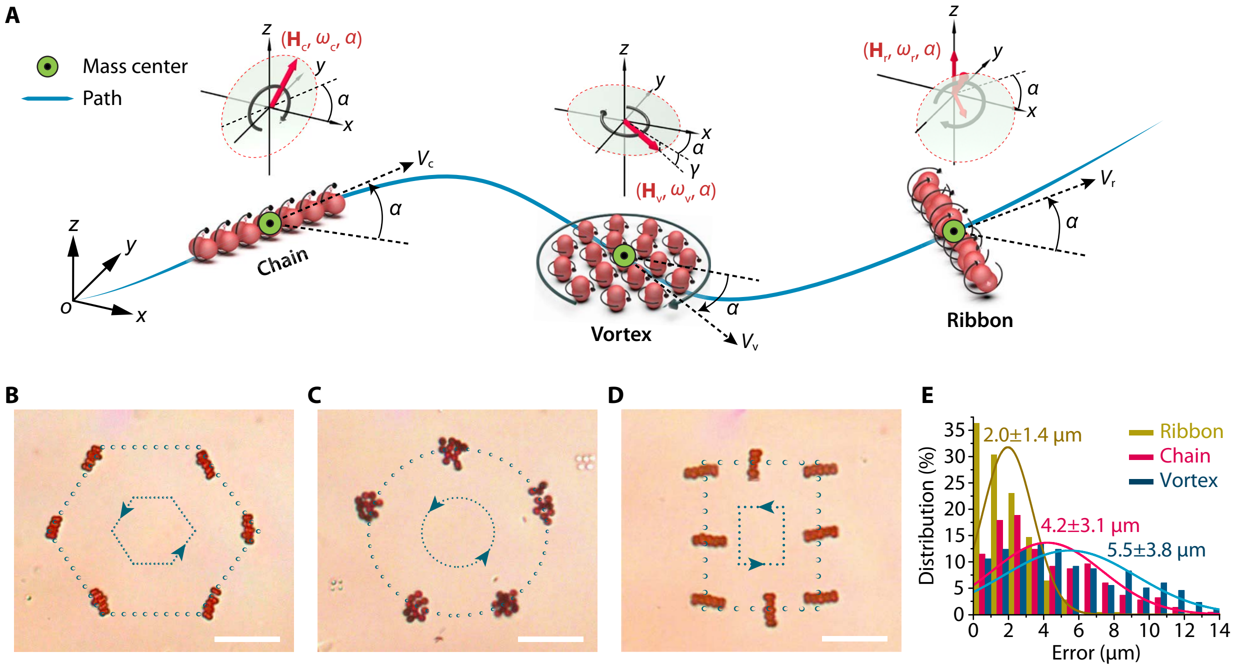

Fig. 7. Programmable swarm locomotion. (**A**) Schematic description of the swarm locomotions of the chain, vortex, and ribbon. Images synthesized by movie screenshots illustrate the locomotion results of the chain (**B**), vortex (**C**), and ribbon (**D**) in tracking planned paths of a pentagon, a circle, and a rectangle, respectively. (**E**) Corresponding distribution histograms showing tracking errors (with SD) of 4.3 ± 3.1 μm, 5.5 ± 3.8 μm, and 2.0 ± 1.4 μm for the chain, vortex, and ribbon, respectively. Scale bars, 20 μm.

Downloaded from https://www.science.org at The Hong Kong University of Science and Technology (Guangzhou) on May 26, 2026

which is comparable to that of the individual microrobot (*37*) or rolling microdevices (*38*).

Environmental adaptability and collective manipulation

To demonstrate manipulation capabilities of the microrobot swarms, we prepared a microfluidic device (Fig. 8A), which mainly consisted of two microcells, named microcell 1 and microcell 2, for aggregating microrobots and performing manipulation tasks, respectively. A narrow channel characterized by a section size of 6 μm by 6 μm and a length of 260 μm was designed to link these two microcells. During the experiment, the microrobots, deposited in the cell 1, must pass through the channel toward the target microcell 2 to complete tasks of collectively handing heavy loads and large-area synchronized manipulation.

We first investigated the interaction between the microrobot and microfluidic wall using the COMSOL Multiphysics Rotating Machinery module. The velocity fields of a microrobot that rotated along its long axis perpendicular (rolling) and parallel (spinning) to a nearby wall were studied (section S9). By analyzing the instantaneous velocity distribution on the plane across the particle center and perpendicular to the long axis, we demonstrate that the flow velocity decreased as the distance from the particle increased, and the smaller the separation between the particle and the wall, the faster the rate of decrease. Similar results were obtained in the simulation of the particles rotating along the short axis (tumbling). It can be understood that the hydrodynamic force and couplings acting on the rotating microrobot exhibited complex behavior when the microrobot was close to the wall (*39*). The motion of the rotating microrobot was substantially suppressed by the viscous resistance introduced by the rigid wall. The magnitude of viscous resistance was not only related to the orientation of the wall with respect to the axis of rotation (*40*) but also increased rapidly as the microrobot got closer to the wall.

Because a microrobotic swarm was formed by a plurality of self-organized microrobots, it naturally interacted with the boundary in the near vicinity. As shown in Fig. 8B, when the vortex encountered a narrowing channel during the movement, it was subjected to a resisting torque from the channel wall, which forced the vortex to change shape or even dissipate, impeding passage through the narrow flow channel as a whole, resulting in inefficient delivery. For the ribbon, the ends near the wall were also subjected to a drag torque from the wall, which hindered its advancement and split it into small ribbons, resulting in low efficiency of delivery. In contrast, the chain could efficiently pass the narrow channel. Although the speed of movement was slightly reduced because of the drag torque from the microfluidic walls, the chain's collective formation could be well maintained because of its shape conforming to the narrow channel.

Inversely, the hydrodynamic flow generated by the swarm has proven to be an effective means for noncontact micromanipulation (*7*). As the simulation results show in Fig. 8C (top), the microfluidic flow induced by the moving vortex was strongly coupled to the boundary of a passive particle in the near vicinity, forming a U-shaped "microfluidic end effector" (the shape of the flow distribution) to push the passive particle. Similarly, as shown in Fig. 8C (bottom), the passive particles could be either pulled or pushed when located behind or in front of the active ribbon (*22*), respectively. The streamplot (Fig. 5C) of the flow velocity profile shows that the fluid approaching the ribbon produced an attractive force, whereas the fluid pulling out created a repulsive force. This was experimentally investigated by the motion trajectories of the silver tracer particles at different positions relative to the propelling ribbon (Fig. 5E).

The ability of vortex, ribbon, and chain microrobot swarms in passing through the narrow channel (see movie S12) was first tested. As shown in the Fig. 8D (left), because of strong interactions between the sidewall and the vortex, even a small vortex with several microrobots had difficulty entering the narrow channel, and a phenomenon occurred in which multiple vortices merged at the entrance of the channel and a blockage was formed. A similar phenomenon occurred when the microrobots were reconfigured in the ribbon formation (Fig. 8D, middle). Although the ribbon (angular velocity ω_v) can break into small ribbons (two to three microrobots) to pass through the narrow channel, the efficiency is very low. For the above two swarm formations, even after a long period (more than a few minutes), only a small number of microrobots reached microcell 2. As shown in Fig. 8D (right), the microrobot swarm in the chain formation proved able to successfully pass through the narrow channel within 70 s and reach the destination cell. The chain smoothly passed through the intersection of two narrow roads with high stability (34 s), although the boundary conditions at this site changed a lot.

The hydrodynamic flow induced by the microrobot swarm, as demonstrated in the simulation results (Fig. 8C), can be applied for collective manipulation to emulate the nature swarms. Before the manipulation experiment, the glass cover of the microfluidic device was removed to accommodate large objects being manipulated at a height exceeding that of the microcell. Once a significant number of microrobots reached microcell 2, they were triggered into ribbon or vortex swarms to perform different tasks by regulating the driving magnetic field. As shown in Fig. 8E (left), the colony-like vortex microrobot swarm was demonstrated to push a polystyrene (PS) microsphere with a diameter of 40 μm that is about 40,000 times the volume of an individual microrobot. At the beginning, the microsphere could not be moved by a vortex with a small number of members; however, when more vortices or member microrobots joined, the microsphere was eventually successfully moved (movie S13). This process is similar to the ant colony cooperatively carrying heavy foods that exceed the ability of individual ants. In contrast, the carrying ability of the ribbon swarm was less than that of the vortex, but it could perform large-area manipulation in a synchronized manner. As shown in Fig. 8E (right), because of the fluidic flow induced by the ribbon, the procession achieved parallel manipulation of multiple microspheres (PS, 8 μm in diameter) by pushing or pulling manners. During this process, the microspheres that were not manipulated or lost by the front ribbon would continue to be manipulated by the following ribbon, just like the synchronized hunting of a herring school.

DISCUSSION

Our results demonstrate that a single species of magnetic microrobots has the potential to produce a variety of active states to address environmental variations or multitasking requirements. By using programmed alternating magnetic fields, the strategy presented here was capable of reconfiguring magnetic microrobots into multiple formations and achieving reversible transformation between these formations. We identified and characterized four main collective formations—liquid, chain, vortex, and ribbon—as well as the transitions from one to another. The unique characteristics of each collective state were detailed, including the periodic motion of microrobots in a chain, the controlled chirality of a vortex, the fusion of vortices, and the fluid profile of the ribbon. The main experimental phenomena were accurately reproduced by the developed computational model, based on the characterization

Downloaded from https://www.science.org at The Hong Kong University of Science and Technology (Guangzhou) on May 26, 2026

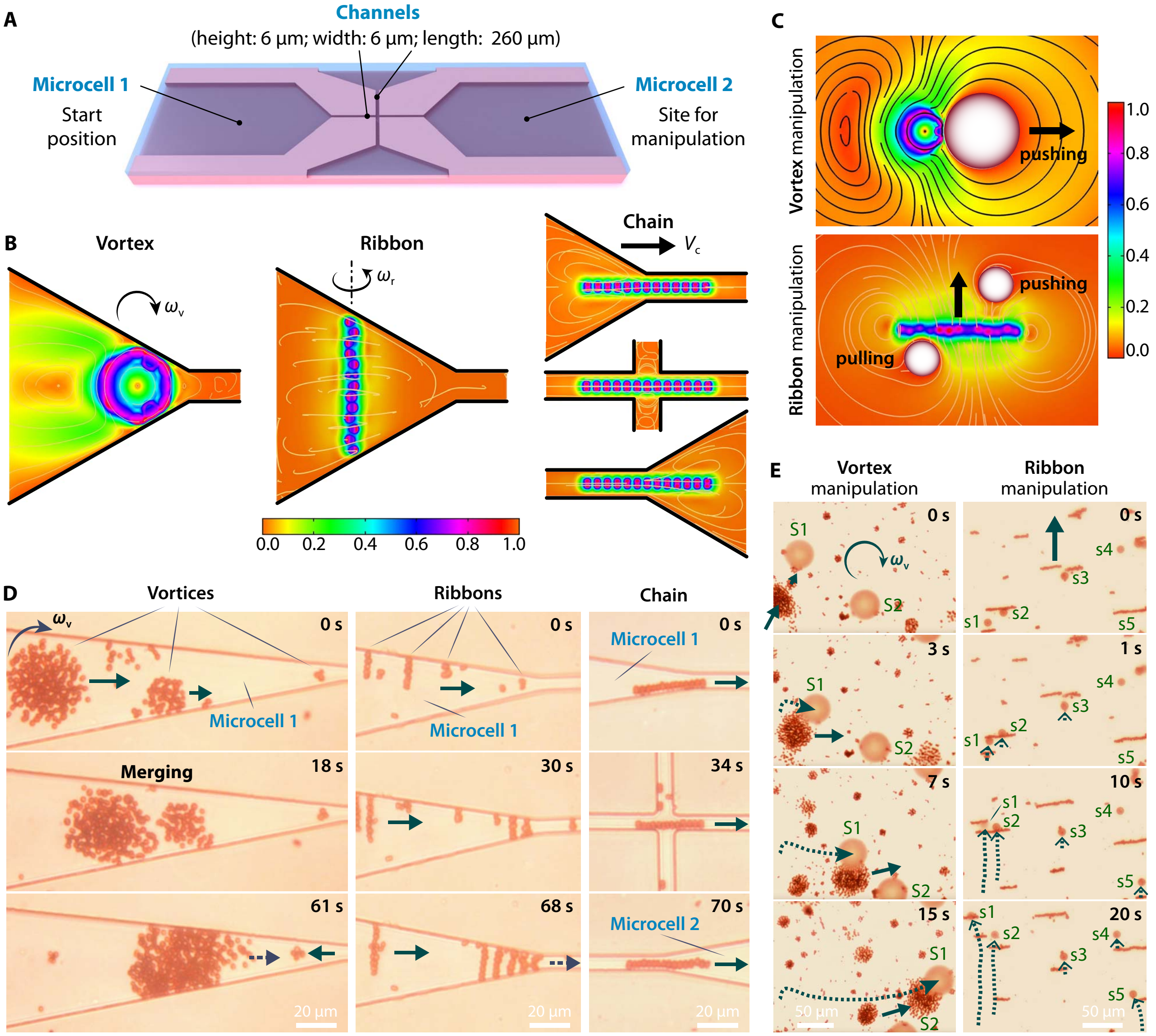

Fig. 8. Environmental adaptability and manipulation of the microrobot swarm. (**A**) Schematic description of the microfluidic device for experiments. Two microcells, named microcell 1 and microcell 2, were designed as sites for aggregating microrobots and performing the manipulation task, respectively. To complete the task, the microrobots must pass through a narrow channel (height, 6 μm; width, 6 μm; length, 260 μm) that links the microcells. (**B**) Microfluidics simulation results of the flow velocity field around the vortex (left), ribbon (middle), and chain (right). (**C**) Microfluidics simulation results of the flow velocity fields of the vortex and ribbon in micromanipulation of passive microparticles. (**D**) Experiments demonstrate that microrobots organized in a vortex (left) and ribbon (middle) were hard to pass through the narrow channel, whereas microrobots in the chain formation (right) were easy to pass. (**E**) Snapshots showing manipulation of PS microsphere (S1; diameter, 40 μm) by a vortex swarm (left) and synchronized manipulation of Ag microspheres (marked with s1 to s5; diameter, 8 μm) by the ribbon swarm (right).

Downloaded from https://www.science.org at The Hong Kong University of Science and Technology (Guangzhou) on May 26, 2026

of particle interactions. High environmental adaptability and multitasking capabilities of the microrobotic swarms were demonstrated by passage through narrow channels (chain formation), coordinated handling of large loads (vortex formation), and large-area synchronized manipulation (ribbon formation). In summary, we have theoretically supported and experimentally demonstrated the idea of achieving the control of a variety of synthetic and living active matter via a programmed external stimulus, thus increasing the possibilities of emulating living systems by active matter. Moreover, the physical mechanisms that govern the dynamics of out-of-equilibrium colloidal systems were carefully investigated, which is helpful for achieving a better understanding of the cooperative mechanisms and self-organization phenomena that occur in active systems; this provides potential solutions for biomedical applications, such as imaging and targeted drug delivery.

MATERIALS AND METHODS

Materials and experimental details

The peanut-shaped microrobots were synthesized on the basis of a previously reported work (*26*). Before magnetic drive experiments, the synthesized microrobots were subjected to an ultrasonic bath for 3 to

5 min. Then, the microrobots were dispersed into a container (filled with deionized water) with a flat bottom (polydimethylsiloxane) and a glass cover. The container was mounted on a microscope stage (Olympus BX-URA2 with objectives 20× and 40×). The trajectories of the microrobots were captured by a fast camera (Pixelink PL-B724F-R). Experiments were performed on the developed software based on the LabVIEW platform, and data analysis was mainly performed using ImageJ and MATLAB.

Magnetic dipole forces

When a pair of microrobots, α and β, are at a distance of $r_{\alpha\beta} = |r_\alpha - r_\beta|$ from one another, the magnetic dipolar interaction between them is given by (*41*)

$$U_{\alpha\beta} = \frac{\mu_0}{4\pi}\left[\frac{\mathbf{m}_\alpha \cdot \mathbf{m}_\beta}{r_{\alpha\beta}^3} - 3\frac{(\mathbf{m}_\alpha \cdot \mathbf{r}_{\alpha\beta})(\mathbf{m}_\beta \cdot \mathbf{r}_{\alpha\beta})}{r_{\alpha\beta}^5}\right] \tag{3}$$

where m_α and m_β are the magnetic dipole moments of microrobot α and β, respectively. Thus, the magnetic force between them can be calculated as

$$\mathbf{F}_{\alpha\beta}^{\mathrm{m}} = -\nabla U_{\alpha\beta} = \frac{3\mu_0}{4\pi r_{\alpha\beta}^5}\left[(\mathbf{m}_\alpha \cdot \mathbf{r}_{\alpha\beta})\mathbf{m}_\beta + (\mathbf{m}_\beta \cdot \mathbf{r}_{\alpha\beta})\mathbf{m}_\alpha + (\mathbf{m}_\alpha \cdot \mathbf{m}_\beta)\mathbf{r}_{\alpha\beta} - 5\frac{(\mathbf{m}_\alpha \cdot \mathbf{r}_{\alpha\beta})(\mathbf{m}_\beta \cdot \mathbf{r}_{\alpha\beta})}{r_{\alpha\beta}^2}\mathbf{r}_{\alpha\beta}\right] \tag{4}$$

where ∇ represents the gradient operator. The microrobots are considered to be uniform spheres of the same size and magnetic dipole moment. When flocking, each microrobot can create a mutual magnetic force that is exerted on the other microrobots. Therefore, the total magnetic force $\mathbf{F}^{\mathrm{m}}$ on a microrobot is the sum of the magnetic forces generated from the remaining $N - 1$ microrobots.

Gravitational force and repulsive electrostatic force

The gravitational force $F^{\mathrm{g}} = \Delta\rho g V$ and the repulsive electrostatic force $F^{\mathrm{e}} = (\zeta/\lambda)e^{-z/\lambda}$ are a pair of opposite forces whose net force compels the microrobot to remain in equilibrium. Here, V is the volume of the microrobot, Δρ (4.24 g cm^{-3}) is defined as the density difference between the microrobot (5.24 g cm^{-3}) and water, λ is the Debye length, and ζ is a surface charge density-dependent prefactor. Therefore, when the microrobots are sprinkled into a liquid environment, after a few minutes, they will suspend above the bottom boundary by a distance h, with $\mathbf{F}^{\mathrm{e}}$ and $\mathbf{F}^{\mathrm{g}}$ reaching a balance. In addition, when the microrobot floated up and down near the equilibrium position, with a small offset **d**, we could derive an effective elastic force to describe the resultant force of those two forces, using the coupling constant $K = gV\Delta\rho/\lambda$ reported in a previous study (*42*). Thus, the net force of $\mathbf{F}^{\mathrm{e}}$ and $\mathbf{F}^{\mathrm{g}}$ (vertical force) for the microrobot can be given by $\mathbf{F}^{\mathrm{n}} = K \cdot \mathbf{d}$.

Hydrodynamic interactions

Hydrodynamic interactions are caused by the fluid field in which a microrobot is located. For a solid sphere that rotates above a solid surface, the solid-liquid boundary can be equivalent to an image system, namely, a hydrodynamic singularity located below the boundary at the same distance. The hydrodynamic singularity is usually composed of a sphere that rotates in the opposite direction, with source doublets and additional stresslet (the sphere's rotating plane is perpendicular to the wall), or it can be composed of the first item (the sphere's rotating plane is perpendicular to the wall). With this assumption, the exact solution of the flow **u** for a rotlet induced by a microrobot with a radius of a, a rotational angular velocity of Ω, and a distance h from the stationary plane boundary is the following (*43*)

$$u = a^3\left[\frac{\varepsilon_{ijk}\Omega_j r_k}{|r|^3} - \frac{\varepsilon_{ijk}\Omega_j R_k}{|R|^3} + 2h\varepsilon_{kjz}\Omega_j\left(\frac{\delta_{ik}}{|R|^3} - \frac{3R_iR_k}{|R|^5}\right) + 6\varepsilon_{kjz}\frac{\Omega_j R_i R_k R_z}{|R|^5}\right] \tag{5}$$

where u is the velocity vector, $r = \sqrt{(x-x_1)^2 + (y-y_1)^2 + (z-z_1)^2}$ is the position from the center of the microrobot, $R = \sqrt{(x-x_1)^2 + (y-y_1)^2 + (z+z_1)^2}$ is the position of its image, (x_1, y_1, z_1) and (x, y, z) are the locations of the microrobot and target position for the fluid velocity calculation, respectively, and ε is the Levi-Civita tensor. When Re ≪ 1, the superposition of fundamental solutions becomes available because the Stokes equations are reduced to a linear equation (*44*). Thus, at any point in a multirotator system, the complete flow field is the superposition of the flow field caused by all of the members. The velocity of the fluid flowing over the surface of each microrobot can be obtained to estimate the thrust force by $F^{\mathrm{t}} = 6\pi\eta a \cdot u$; here, $\eta = 1 \times 10^3$ Pa · s is the viscosity of the flow.

There is also a repulsive force between the rotating microrobots. The low Reynolds number hydrodynamics can be used to reveal the source of repulsion. The hydrodynamic repulsion $\mathbf{F}^{\mathrm{r}}$ that one microrobot exerts on another microrobot depends on the radius a, the rotational speed Ω, the distance d between their centers, and the density of the fluid ρ. F^{r} is proportional to $\rho\Omega^2a^7/d^3$, and it acts along the direction of d and away from other microrobots (*45*).

In addition to the thrust force and repulsive force, the vortex exerts long-range attracting forces on other rotating systems (*46*). The attraction is positively correlated with the velocity of the vortex core (linearly correlated with Ω), whereas it is negatively correlated with the distance between the vortices. When a microrobot is inside the core of a vortex, inward trapping forces will be exerted on it (*47*, *48*). In this study, we simply express the vortex's attractive force as $F^{\mathrm{a}} = C \cdot \Omega/r_{\mathrm{c}}$, where C is the scaling factor and r_{c} is the distance from the center of the vortex.

Swarm locomotion

At low Reynolds numbers, the swarms can be modeled as a first-order kinematic system

$$\begin{cases} \dot{x}(t) = v_1(\omega(t)) + b(t) \\ \dot{y}(t) = v_2(\omega(t)) + b(t) \\ \dot{\alpha}(t) = \dot{\beta}(t) \end{cases} \tag{6}$$

with

$$\begin{bmatrix} v_1(\omega(t)) \\ v_2(\omega(t)) \end{bmatrix} = \begin{bmatrix} \cos(\phi(t)) & 0 \\ 0 & \sin(\phi(t)) \end{bmatrix}\begin{bmatrix} k\omega(t) \\ k\omega(t) \end{bmatrix}$$

where k is the ratio between swarm's velocity v and frequency ω of the magnetic field, $b(t)$ is random disturbances and noise from the liquid environment, $\dot{\beta}$ is the steering rate of the input magnetic field, and $\dot{\alpha}$ is the steering rate of the microrobot swarm.

Downloaded from https://www.science.org at The Hong Kong University of Science and Technology (Guangzhou) on May 26, 2026

SUPPLEMENTARY MATERIALS

robotics.sciencemag.org/cgi/content/full/4/28/eaav8006/DC1
Section S1. Experimental setup
Section S2. Calculation of the pair correlation function
Section S3. Hydrodynamic coupling in chain
Section S4. Motion trajectories of a quat-microrobot chain
Section S5. Giant number fluctuations in vortices
Section S6. Velocity field of a vortex
Section S7. Merging process of a giant vortex
Section S8. Closed-loop controller for swarm locomotion
Section S9. Simulation results of a microrobot that interacts with the microfluidics wall
Fig. S1. Experimental setup system.
Fig. S2. Calculation of the pair correlation function.
Fig. S3. Simulation of hydrodynamic coupling in chain.
Fig. S4. Motion trajectory simulation.
Fig. S5. Magnitude of the velocity fields.
Fig. S6. State of the vortex.
Fig. S7. Merging process of a giant vortex.
Fig. S8. Closed-loop controller.
Fig. S9. Microfluidics simulation results of a rotating peanut-shaped particle.
Movie S1. Four swarm formations of microrobots.
Movie S2. Generation and motion trajectory simulation of the chain.
Movie S3. Generation and chirality switch of the vortex.
Movie S4. Vortex merging.
Movie S5. Generation of a giant vortex.
Movie S6. Generation and the flow field of a ribbon.
Movie S7. Transformations of the chain from the other three formations.
Movie S8. Transformations of the ribbon from the other three formations.
Movie S9. Transformations of the vortex from the other three formations.
Movie S10. Transformations of the liquid from the other three formations.
Movie S11. Swarm locomotion.
Movie S12. Environmental adaptability.
Movie S13. Collective manipulation.
Reference (*49*)

REFERENCES AND NOTES

1. E. O. Wilson, The sociogenesis of insect colonies. *Science* **228**, 1489–1495 (1985).
2. A. Gelblum, I. Pinkoviezky, E. Fonio, A. Ghosh, N. Gov, O. Feinerman, Ant groups optimally amplify the effect of transiently informed individuals. *Nat. Commun.* **6**, 7729 (2015).
3. M. Rubenstein, A. Cornejo, R. Nagpal, Programmable self-assembly in a thousand-robot swarm. *Science* **345**, 795–799 (2014).
4. R. Groß, M. Bonani, F. Mondada, M. Dorigo, Autonomous self-assembly in swarm-bots. *IEEE Trans. Robot.* **22**, 1115–1130 (2006).
5. L. Garattoni, M. Birattari, Autonomous task sequencing in a robot swarm. *Sci. Rob.* **3**, eaat0430 (2018).
6. J. Li, B. E.-F. de Ávila, W. Gao, L. Zhang, J. Wang, Micro/nanorobots for biomedicine: Delivery, surgery, sensing, and detoxification. *Sci. Robot.* **2**, eaam6431 (2017).
7. J. Yu, B. Wang, X. Du, Q. Wang, L. Zhang, Ultra-extensible ribbon-like magnetic microswarm. *Nat. Commun.* **9**, 3260 (2018).
8. A. Bricard, J.-B. Caussin, D. Das, C. Savoie, V. Chikkadi, K. Shitara, O. Chepizhko, F. Peruani, D. Saintillan, D. Bartolo, Emergent vortices in populations of colloidal rollers. *Nat. Commun.* **6**, 7470 (2015).
9. J. Yan, M. Bloom, S. C. Bae, E. Luijten, S. Granick, Linking synchronization to self-assembly using magnetic Janus colloids. *Nature* **491**, 578–581 (2012).
10. J. Yan, S. C. Bae, S. Granick, Colloidal superstructures programmed into magnetic Janus particles. *Adv. Mater.* **27**, 874–879 (2015).
11. J. Yan, M. Han, J. Zhang, C. Xu, E. Luijten, S. Granick, Reconfiguring active particles by electrostatic imbalance. *Nat. Mater.* **15**, 1095–1099 (2016).
12. M. E. Leunissen, H. R. Vutukuri, A. van Blaaderen, Directing colloidal self-assembly with biaxial electric fields. *Adv. Mater.* **21**, 3116–3120 (2009).
13. J. Palacci, S. Sacanna, A. P. Steinberg, D. J. Pine, P. M. Chaikin, Living crystals of light-activated colloidal surfers. *Science* **339**, 936–940 (2013).
14. F. J. Nédélec, T. Surrey, A. C. Maggs, S. Leibler, Self-organization of microtubules and motors. *Nature* **389**, 305–308 (1997).
15. T. Vicsek, A. Czirók, E. Ben-Jacob, I. Cohen, O. Shochet, Novel type of phase transition in a system of self-driven particles. *Phys. Rev. Lett.* **75**, 1226–1229 (1995).
16. G. Grégoire, H. Chaté, Onset of collective and cohesive motion. *Phys. Rev. Lett.* **92**, 025702 (2004).
17. F. Ginelli, F. Peruani, M. Bär, H. Chaté, Large-scale collective properties of self-propelled rods. *Phys. Rev. Lett.* **104**, 184502 (2010).
18. F. Guzmán-Lastra, A. Kaiser, H. Löwen, Fission and fusion scenarios for magnetic microswimmer clusters. *Nat. Commun.* **7**, 13519 (2016).
19. J. Deseigne, O. Dauchot, H. Chaté, Collective motion of vibrated polar disks. *Phys. Rev. Lett.* **105**, 098001 (2010).
20. F. Ma, S. Wang, D. T. Wu, N. Wu, Electric-field–induced assembly and propulsion of chiral colloidal clusters. *Proc. Natl. Acad. Sci. U.S.A.* **112**, 6307–6312 (2015).
21. I. Buttinoni, J. Bialké, F. Kümmel, H. Löwen, C. Bechinger, T. Speck, Dynamical clustering and phase separation in suspensions of self-propelled colloidal particles. *Phys. Rev. Lett.* **110**, 238301 (2013).
22. S. Hernàndez-Navarro, P. Tierno, J. A. Farrera, J. Ignés-Mullol, F. Sagués, Reconfigurable swarms of nematic colloids controlled by photoactivated surface patterns. *Angew. Chem. Int. Ed. Engl.* **53**, 10696–10700 (2014).
23. A. Kaiser, A. Snezhko, I. S. Aranson, Flocking ferromagnetic colloids. *Sci. Adv.* **3**, e1601469 (2017).
24. A. Bricard, J.-B. Caussin, N. Desreumaux, O. Dauchot, D. Bartolo, Emergence of macroscopic directed motion in populations of motile colloids. *Nature* **503**, 95–98 (2013).
25. A. Snezhko, I. S. Aranson, Magnetic manipulation of self-assembled colloidal asters. *Nat. Mater.* **10**, 698–703 (2011).
26. M. Driscoll, B. Delmotte, M. Youssef, S. Sacanna, A. Donev, P. Chaikin, Unstable fronts and motile structures formed by microrollers. *Nat. Phys.* **13**, 375–379 (2017).
27. F. Martinez-Pedrero, A. Ortiz-Ambriz, I. Pagonabarraga, P. Tierno, Colloidal microworms propelling via a cooperative hydrodynamic conveyor belt. *Phys. Rev. Lett.* **115**, 138301 (2015).
28. Z. Lin, T. Si, Z. Wu, C. Gao, X. Lin, Q. He, Light-activated active colloid ribbons. *Angew. Chem. Int. Ed.* **129**, 13702–13705 (2017).
29. H. Massana-Cid, F. Martinez-Pedrero, E. Navarro-Argemí, I. Pagonabarraga, P. Tierno, Propulsion and hydrodynamic particle transport of magnetically twisted colloidal ribbons. *New J. Phys.* **19**, 103031 (2017).
30. J. Yan, S. C. Bae, S. Granick, Rotating crystals of magnetic Janus colloids. *Soft Matter* **11**, 147–153 (2015).
31. G. Kokot, A. Snezhko, Manipulation of emergent vortices in swarms of magnetic rollers. *Nat. Commun.* **9**, 2344 (2018).
32. E. M. Purcell, Life at low Reynolds number. *Am. J. Phys.* **45**, 3–11 (1977).
33. P. Tierno, J. Claret, F. Sagués, A. Cēbers, Overdamped dynamics of paramagnetic ellipsoids in a precessing magnetic field. *Phys. Rev. E* **79**, 021501 (2009).
34. Q. Zhou, T. Petit, H. Choi, B. J. Nelson, L. Zhang, Dumbbell fluidic tweezers for dynamical trapping and selective transport of microobjects. *Adv. Funct. Mater.* **27**, 1604571 (2017).
35. I. Theurkauff, C. Cottin-Bizonne, J. Palacci, C. Ybert, L. Bocquet, Dynamic clustering in active colloidal suspensions with chemical signaling. *Phys. Rev. Lett.* **108**, 268303 (2012).
36. Y. Fily, M. C. Marchetti, Athermal phase separation of self-propelled particles with no alignment. *Phys. Rev. Lett.* **108**, 235702 (2012).
37. Z. Lin, X. Fan, M. Sun, C. Gao, Q. He, H. Xie, Magnetically actuated peanut colloid motors for cell manipulation and patterning. *ACS Nano* **12**, 2539–2545 (2018).
38. T. O. Tasci, P. S. Herson, K. B. Neeves, D. W. M. Marr, Surface-enabled propulsion and control of colloidal microwheels. *Nat. Commun.* **7**, 10225 (2016).
39. Q. Liu, A. Prosperetti, Wall effects on a rotating sphere. *J. Fluid Mechanics* **657**, 1–21 (2010).
40. F. Box, K. Singh, T. Mullin, The interaction between rotationally oscillating spheres and solid boundaries in a stokes flow. *J. Fluid Mechanics* **849**, 834–859 (2018).
41. S. Melle, O. G. Calderón, M. A. Rubio, G. G. Fuller, Microstructure evolution in magnetorheological suspensions governed by Mason number. *Phys. Rev. E.* **68**, 041503 (2003).
42. F. Martinez-Pedrero, E. Navarro-Argemí, A. Ortiz-Ambriz, I. Pagonabarraga, P. Tierno, Emergent hydrodynamic bound states between magnetically powered micropropellers. *Sci. Adv.* **4**, eaap9379 (2018).
43. J. R. Blake, A. T. Chwang, Fundamental singularities of viscous flow. *J. Eng. Math.* **8**, 23–29 (1974).
44. K. E. Peyer, L. Zhang, B. J. Nelson, Bio-inspired magnetic swimming microrobots for biomedical applications. *Nanoscale* **5**, 1259–1272 (2013).
45. B. A. Grzybowski, X. Jiang, H. A. Stone, G. M. Whitesides, Dynamic, self-assembled aggregates of magnetized, millimeter-sized objects rotating at the liquid-air interface: Macroscopic, two-dimensional classical artificial atoms and molecules. *Phys. Rev. E.* **64**, 011603 (2001).
46. J. Yu, T. Xu, Z. Lu, C. I. Vong, L. Zhang, On-demand disassembly of paramagnetic nanoparticle chains for microrobotic cargo delivery. *IEEE. Trans. Robot.* **33**, 1213–1225 (2017).
47. J. Yu, L. Yang, L. Zhang, Pattern generation and motion control of a vortex-like paramagnetic nanoparticle swarm. *Int. J. Robot. Res* **37**, 912–930 (2018).
48. T. Petit, L. Zhang, K. E. Peyer, B. E. Kratochvil, B. J. Nelson, Selective trapping and manipulation of microscale objects using mobile microvortices. *Nano Lett.* **12**, 156–160 (2011).

Downloaded from https://www.science.org at The Hong Kong University of Science and Technology (Guangzhou) on May 26, 2026

49. L. Angelani, C. Maggi, M. L. Bernardini, A. Rizzo, R. Di Leonardo, Effective interactions between colloidal particles suspended in a bath of swimming cells. *Phy. Rev. Lett.* **107**, 138302 (2011).

Funding: This work was partially supported by the National Key Research and Development Programme of China (grant no. 2018YFB13049030), the National Natural Science Foundation of China (grant no. 61573121), and the Beijing Advanced Innovation Center for Intelligent Robots and Systems (grant no. 2018IRS02). L.D. thanks the Beijing Institute of Technology for hosting him as a visiting professor during his sabbatical leave, which has enabled this collaborative work from his side.

Author contributions: H.X., Q.H., and L.D. conceived the idea and designed the research. H.X., M.S., and X.F. coanalyzed the experimental and calculated data. W.C. and Z.L. prepared the magnetic colloidal particles. L.W. prepared the experimental devices. H.X. directed the project. H.X., M.S., X.F., Q.H., and L.D. contributed to the writing and editing of the manuscript. **Competing interests:** The authors declare that they have no competing interests. **Data and materials availability:** All data are provided in the manuscript and the Supplementary Materials. Contact H.X. for materials.

Submitted 21 October 2018
Accepted 8 February 2019
Published 20 March 2019
10.1126/scirobotics.aav8006

Citation: H. Xie, M. Sun, X. Fan, Z. Lin, W. Chen, L. Wang, L. Dong, Q. He, Reconfigurable magnetic microrobot swarm: Multimode transformation, locomotion, and manipulation. *Sci. Robot.* **4**, eaav8006 (2019).

Downloaded from https://www.science.org at The Hong Kong University of Science and Technology (Guangzhou) on May 26, 2026

Science Robotics

Reconfigurable magnetic microrobot swarm: Multimode transformation, locomotion, and manipulation

Hui Xie, Mengmeng Sun, Xinjian Fan, Zhihua Lin, Weinan Chen, Lei Wang, Lixin Dong, and Qiang He

Sci. Robot. **4** (28), eaav8006. DOI: 10.1126/scirobotics.aav8006

View the article online
https://www.science.org/doi/10.1126/scirobotics.aav8006
Permissions
https://www.science.org/help/reprints-and-permissions

Downloaded from https://www.science.org at The Hong Kong University of Science and Technology (Guangzhou) on May 26, 2026

Use of this article is subject to the Terms of service

Science Robotics (ISSN 2470-9476) is published by the American Association for the Advancement of Science. 1200 New York Avenue NW, Washington, DC 20005. The title *Science Robotics* is a registered trademark of AAAS.

Copyright © 2019 The Authors, some rights reserved; exclusive licensee American Association for the Advancement of Science. No claim to original U.S. Government Works